Nanobody-guided redox and enzymatic functionalization of icosahedral virus particles for enhanced bioelectrocatalysis

Racha Kassem, Anne Cousin, Daniel Clesse, Vianney Poignavent, Adrien Trolet, Christophe Ritzenthaler, Thierry Michon, Arnaud Chovin, Christophe Demaille

Nanobody-Guided Redox and Enzymatic Functionalization of Icosahedral Virus Particles for Enhanced Bio-Electro-Catalysis

Racha Kassem[1], Anne Cousin[3], Daniel Clesse[3], Vianney Poignavent[3], Adrien Trolet[3], Christophe Ritzenthaler[3], Thierry Michon*[2], Arnaud Chovin*[1], Christophe Demaille*[1]*

[1] Université Paris Cité, CNRS, Laboratoire d'Electrochimie Moléculaire, F-75013 Paris, France

[2] Université de Bordeaux, Biologie du Fruit et Pathologie, INRA UMR 1332, F-33140 Villenave d'Ornon, France

[3] Institut de Biologie Moléculaire des Plantes, UPR2357 du Centre National de la Recherche Scientifique, Université de Strasbourg, F-67084 Strasbourg, France

* To whom correspondence should be addressed.

E-mail: arnaud.chovin@ u-paris.fr; christophe.demaille@u-paris.fr ; ritzenth@unistra.fr; thierry.michon@inrae.fr;

Abstract

Icosahedral, 30 nm diameter, *grapevine fanleaf* virus (GFLV) virus particles are adsorbed onto electrodes and used as nanoscaffolds for the assembly of an integrated glucose oxidizing system, comprising the enzyme pyrroloquinoline quinone-glucose dehydrogenase (PQQ-GDH) and ferrocenylated polyethylene glycol chains (Fc-PEG) as a redox cosubstrate. Two different GFLV-specific nanobodies, either fused to the enzyme, or chemically conjugated to Fc-PEG, are used for the regio-selective immunodecoration of the viral particles. A comprehensive kinetic characterization of the enzymatic function of the particles, initially decorated with the enzyme alone shows that simple immobilization on the GFLV capsid has no effect on the kinetic scheme of the enzyme, nor on its catalytic activity. However, we find that co-immobilization of the enzyme *and* the Fc-PEG cosubtrate on GFLV does induce enzymatic enhancement, by promoting cooperativity between the two subunits of the homodimeric enzyme, via "synchronization" of their redox state. A decrease in inhibition of the enzyme by its substrate (glucose) is also observed.

Keywords: PQQ-GDH, Bioscaffolding, Nanoparticle enhanced bioelectrocatalysis, Viral nanotechnology

1. Introduction

Attachment to nanosized scaffolds has been shown to enhance the activity of a wide range of enzymes,[1,2] including hydrolases, [3,4] proteases,[5,6] or oxidoreductases.[7,8]However, despite these findings, the mechanism behind this enhancement and the potential biotechnology applications of this approach still require further research. In early works, inorganic particles such as metallic or semiconducting materials,[5,9,10] have been used as scaffolds to demonstrate enzymatic enhancement. Bioscaffolds, notably DNA nanostructures, including DNA origamis,[11] have also often been employed to evidence the effect of scaffolding, typically on the performances of multi-enzyme complexes,[12–18] but also of simpler systems, comprising a single enzyme type.[8,19] These works have led to the view that, rather than nanoscaffolding *per se*, it is the local microenvironment created by the scaffold which plays a central role in the modulation of enzymatic activity.[19–21] One potential mechanism for this is the binding of the substrate to the scaffold material, which can increase substrate concentration and alter the enzyme's apparent Michaelis constant (K_M) value,[22] or favor substrate inhibition.[23] In addition, local electrostatic charges are also suspected to play a central role, as they can shift the local pH closer to the enzyme's optimal pH.[24] They can also affect enzymatic specificity toward charged substrates,[25] or modulate kinetics through a local ionic-strength effect.[20,21]

Viral particles, which typically display a very high electric charge density and high levels of organization, are therefore good candidates as nanoscaffolds potentially capable of modulating enzymatic activity. Indeed, since the first proposals to use viral particles as enzyme nanocarriers,[26–28] plant virions and bacteriophages (both harmless to humans) have been used to construct enzymatic systems, seeking to improve catalysis. The enzymes were either displayed on the outer surface of the virus particles or encapsulated in the inner cavity. [26,27,29–40] It was found that virus-based nanoscaffolds can improve or protect enzyme activity in many cases, when the virions are dispersed in solution.[30,37,40] However, the use of viral particles as carriers to enhance the catalytic response of *electrode-supported enzymes* has been comparatively little explored.

In early studies, it was reported that adsorption of *tobacco mosaic virus* (TMV) nanotubes functionalized with the redox enzyme glucose oxidase on the surface of a sensor electrode did not improve oxygen-mediated catalysis, but significantly enhanced enzyme loading and sensor reusability.[35,41] Importantly, displaying redox enzymes on nanoscaffolds immobilized on an electrode not only has the potential to enhance enzymatic activity but also to improve the electrical connection between the enzyme's active site and the electrode.[42–46] This applies whether the electron transfer occurs directly or through a co-immobilized redox cosubstrate, in a so-called integrated system configuration.[47,48]

In previous studies,[49–51] we have designed an integrated enzymatic system, which consisted of a glucose-oxidizing enzyme, pyrroloquinoline quinone-glucose dehydrogenase (PQQ-GDH) and ferrocenylated polyethylene glycol chains (Fc-PEG) as a redox co-substrate. This system was immunologically assembled on elongated, sub-micron length *fd*-bacteriophage (~6 nm in diameter and 900 nm long)[49,50] or TMV (18 nm in diameter and 300 nm long)[51] adsorbed on gold electrodes, using antibodies (IgGs) conjugated to the enzyme or to Fc-PEG. We observed that such scaffolding afforded both fast electron transport from the electrode to the enzyme and high catalytic performances.

The current study aims to investigate how assembling the same integrated system on much smaller, ~30 nm icosahedral viral particles of *grapevine fanleaf virus* (GFLV) affects the enzymatic activity of the system. This downscaling is made possible by the use of nanobodies, which are small single-domain antibodies with a molar mass of only one tenth that of an IgG,[52,53] to mediate functionalization of the virions. For this, the nanobodies were either genetically fused to the enzyme or chemically coupled to Fc-PEG. In a detailed and stepwise study, we carefully investigate the effects of scaffolding on the kinetic behavior of the system. We reveal that nano-confinement of the integrated system induces catalytic

enhancement by promoting subunit cooperativity in the enzyme, via a more efficient buffering of its redox state.

2. Material and Methods.

2.1. Biological Material.

Virus-Like Particle (VLP) from GFLV were purified as previously described.[54] Cloning, production and purification of the fusions between: (*i*) nanobody 59 and green fluorescent protein (GFP), Nb_{59}-GFP, and (*ii*) nanobody 75 and pyrroloquinoline quinone-glucose dehydrogenase (GDH), GDH-Nb_{75}, are described in Supplementary Material.

2.2. Chemicals and solutions.

All chemicals were analytical grade Sigma-Aldrich products and used without further purification. The solutions were made using double-deionized water with a resistivity of 18.2 MΩ cm (TKA Micro-Pure UV). Two types of buffer solutions were utilized: 10 mM pH 7 phosphate buffer and 50 mM pH 7.5 Tris-HCl buffer. Phosphate buffer was used to prepare the GFLV and Fc-PEG-Nb_{59}-GFP solutions, while Tris buffer was used for the solution of GDH-Nb_{75}, for the CV characterizations and as the imaging medium for the in-situ AFM experiments. All nanobodies solutions contained typically 1 mg/ml BSA and 0.5 mg/ml B2-GFP. Stock solutions of glucose in Tris buffer were left to mutarotate overnight.

2.3 Kinetic characterization of the GFP-Nb_{75} fusion. See supplementary material, Figure S1 and S2.

2.4 Preparation and characterization of the redox nanobody, Fc-PEG-Nb_{59}-GFP.

Fc-PEG chains were covalently conjugated to Nb_{59}-GFP by reacting the NHS activated ester of a home synthesized NHS-PEG_{3500}-Fc chain[55] with the amino groups of the Nb_{59}-GFP, as previously described.[56] The purified Fc-PEG-Nb_{59}-GFP was found to be decorated with ~ 8 Fc-PEG chains per Nb_{59}-GFP, as determined by UV-vis spectroscopy (Supplementary Material, Figure S3).

2.5 Assembly of the GFLV-scaffolded systems on gold surfaces.

2.5.1 Ultra-flat gold surfaces.

The ultra-flat gold surfaces supporting the GFLV-scaffolded systems were produced by stripping of a 200 nm thick gold layer from mica, either mechanically or with the help of tetrahydrofuran, as previously described.[57]A perforated Teflon adhesive mask was glued onto the surface in order to define a disk-shaped electrode.

2.5.2 Self-assembly of a cysteamine layer on gold surfaces.

A 20 µL drop of a 5 mM cysteamine hydrochloride solution in water was left on gold surface for 2h-adsorption, under water-saturated nitrogen atmosphere. All the further assembly steps were performed under the same inert atmosphere, to avoid oxidative desorption of the cysteamine layer from the gold electrode surface.

2.5.3 Formation of random GFLV arrays on cysteaminated gold surfaces.

20 µL of a 10 mM pH 7 phosphate buffer solution, containing GFLV at a concentration chosen in the 2-30 µg/mL range, was deposited on the cysteaminated gold surface for 20 min. The surface was then rinsed by two droplet replacement steps and left in contact with phosphate buffer for 10 min, to desorb any weakly bound material. This resulted in the formation of random arrays of irreversibly adsorbed GFLV on gold surfaces, displaying a reproducible surface coverage, which increased with the initial GFV concentration in the adsorption solution ("isotherm" in Supplemental Material, Figure S4). The

surface was then backfilled with sequential 30 min treatment with 2 mg/mL Bovine Serum Albumin (BSA) and 1 mg/mL B2-GFP protein, to block non-specific adsorption during the next assembly steps.

2.5.4 Assembly of the GDH-Nb_{75} fusion.

20 µL of a 15 µg/mL anti-GFLV GDH-Nb_{75} conjugate in Tris buffer was put in contact with the surface for 2 h. A double 5 min rinsing/desorption step was performed in the same buffer solution containing 1 mg/mL BSA and 0.5mg/ml B2-GFP.

2.5.5 Assay of the number of GDH molecules decorating GFLV virions.

See Supplementary material.

2.5.6 Assembly of the Fc-PEG-Nb_{59}-GFP nanobody.

The BSA/B2-GFP backfilled GFLV-bearing surface was incubated with 20 µL of 16 µg/mL Fc-PEG-Nb_{59}-GFP solution overnight. After that, 2 rinsing/desorption steps of 5 min each were carried out using phosphate buffer solution containing 1 mg/mL BSA and 0.5 mg/ml B2-GFP, followed by two droplet replacement rinsing and desorption steps of 10 min.

2.5.7 AFM imaging.

Before AFM imaging the GFLV-bearing surfaces were treated with 1% glutaraldehyde in a 10 mM pH 7 phosphate buffer for 20 min. This fixative agent rigidified the particles, making them easier to image. Imaging had thus to be carried out after all of the assembly and characterization steps were completed. We made sure, by imaging test surfaces at various stages of the experiments, that the virion coverage on the surface remained constant throughout these steps. Tapping mode AFM images were acquired with a Nanowizard II microscope (JPK, Germany). *In situ* imaging (in phosphate or Tris buffer) was carried out with soft home-made gold tips prepared from a 25 µm diameter etched and flatted gold wire, characterize by a spring constant less than 0.1 N/m.[50] *In air* imaging was performed after rinsing the surface with water and drying, using a Multi75G commercial tip with a specific spring constant 3 N/m and frequency of 75 kHz. Both conditions yielded similar results (notably in terms of virus count) albeit imaging in air was easier.

2.5.8 Electrochemical analysis.

The surface bearing the decorated GFLV was mounted in a standard JPK electrochemical liquid cell. Cyclic and square wave voltammograms (CVs and SWVs) were recorded with a CHI630C electrochemical workstation, in a three electrode configuration, using the platinum wire counter electrode of the JPK cell, and a standard KCl-saturated calomel electrode (SCE) inserted in the middle of the cell. Temperature of the air-conditioned room was around 22 °C. We systematically ensured that all signals were stable to potential cycling. For each experimental conditions three electrodes were engaged, including one that did not carry GFLV and used as a blank. Measurements from the two other electrodes were typically found to be within ± 20% and averaged.

3. Results and Discussion

3.1. Assembly of a random array of electrocatalytic GFLV particles on an ultraflat gold electrode.

The choice of GFLV as a nanoscaffold was motivated first by its small size (30 nm in diameter) and quasi-spherical (icosahedral) geometry providing a high degree of spatial confinement for the enzymatic system,[58,59] prone to favor catalytic enhancement, Figure 1A. In addition, GFLV is unique in the capacity of its capsid protein to accommodate N- and C-terminal fusions, allowing encaging or display of entire proteins in the particle interior cavity or outer surface, respectively.[60] Finally, Nanobodies (Nbs) derived

from camelid heavy chain immunoglobulins with high affinity and specificity against GFLV are available.[61,62] Nanobodies display molecular recognition capabilities similar to antibodies, but with a molecular weight of only 15 kDa.[63] They are oblong tiny objects, 2.5 nm in diameter and 4 nm in length, which renders them ideal for efficiently decorating surface-adsorbed GFLV with, *a priori*, little steric constraints.

For our study, random arrays of electrocatalytic GFLV particles were formed on template-stripped (TS) gold electrode surfaces, as depicted in Figure 1B and detailed below.

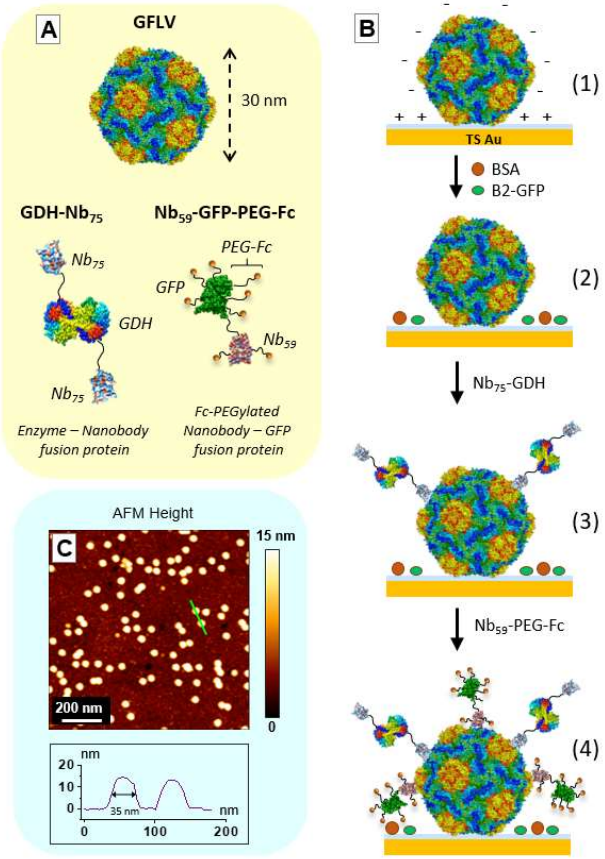

Figure 1. Assembly of a random array of electrocatalytic GFLV particles on an ultraflat TS gold electrode surface. (A) Depiction of the molecular components of the system. (B) Schematics of the assembly steps. (C) Tapping mode imaging in air of the array of the electrocatalytic GFLV particles. In (B) the GFLV and the fusion proteins are drawn to scale

Purified GFLV particles at various concentrations (from 2-30 µg/mL) in 10 mM pH 7.0 phosphate buffer were put in contact with a TS gold surface, carrying a positively charged pre-self-assembled layer of cysteamine, allowing irreversible adsorption of the virions on the surface. The presence of GFLV on the surface could be monitored by AFM microscopy, recorded in liquid, or in air for test surfaces not engaged in further assembly steps (Figure 1C). The images showed numerous spherical objects ascribable to virions, their surface coverage, γ_{vir}, could then be derived by simple counting. γ_{vir} could be tuned by adjusting the concentration of GFLV in the adsorption solution, referring to an "adsorption isotherm" plot we built experimentally (Supplementary material).

Surface sites left free after GFLV adsorption were blocked by the sequential adsorption of bovine serum albumin (BSA) and of B2-GFP purified from *E. coli*. This latter protein is a genetic fusion between the double-stranded RNA-binding domain of the protein B2 from flock house virus and the enhanced green fluorescent protein (GFP), which was selected here solely for its high solubility, small size (36

kDa) and superior blocking property.[64] Several other, more classical blocking agents and protocols were either found to be incompatible with the assembly of the GFLV array or to provide insufficient anti-fouling activity against non-specific adsorption of the reagents subsequently used in the assembly process (Table S1 in Supplementary Material).

In order to assemble the "active" macromolecular components of the integrated system, i.e. PQQ-GDH enzyme and Fc-PEG chains, on such a small scaffold as GFLV, in a spatially controlled way, we made use of two Nbs, Nb_{75} and Nb_{59} nanobodies, each able to recognize distinct conformational epitopes at the GFLV surface.[62]

We first made use of a genetic fusion between PQQ-GDH and Nb_{75} (GDH-Nb_{75} hereafter). To do so, the C-terminus of *Acinetobacter calcoaceticus* PQQ-GDH, which is freely accessible at the enzyme outer surface (https://doi.org/10.2210/pdb1C9U/pdb), was fused to the N-terminus of Nb_{75} (Supplementary Material for details). To avoid steric hindrance, we added a flexible linker with the sequence $(GGGGS)_2GGGS$ between the nanobody and enzyme chains. The active PQQ-GDH being a homodimer,[65] this ultimately resulted in the formation of an apoenzyme consisting of a GDH-Linker-Nb_{75} dimer of 130 kDa (Figure 1A) which was expressed and purified from *E. coli* under native conditions. Note that genetic fusion was preferred over stochastic chemical coupling of GDH to Nb to maintain optimal activity of both GDH and Nb_{75}. Indeed, we observed that the enzymatic activity of GDH-Nb_{75} in solution, once converted into its holo-form by PQQ incorporation, was the same as that of native PQQ-GDH Supplementary Material).

The purified GDH-Nb_{75} enzyme was then incubated with GFLV particles adsorbed at the surface of BSA/B2-GFP coated gold surfaces. The concentration and exposure time were chosen so as to be sufficient for the GDH-Nb_{75} binding to reach saturation (16 µg/ml, ~ 20 min). Incorporation of the Fc-PEG co-substrate was carried out subsequently by using a "redox-nanobody", consisting of a Nb_{59}-GFP genetic fusion purified from *E. coli* and further functionalized with Fc-PEG_{3400} chains by chemical coupling. As Fc-PEG carrier, we opted for a Nb_{59}-GFP fusion instead of Nb_{59} only. The aim here was to minimize potential loss of the Nb_{59} binding capacities to GFLV upon attachment of the bulky (5 nm Flory radius) PEG chains. In addition, the secondary amine-targeted chemical conjugation of Fc-PEG-NHS chains was preferentially directed toward GFP rather than Nb_{59}, as the former displays many more lysine groups than the latter (19 vs. 6). UV-spectroscopy characterization of the Fc-PEG-Nb_{59}-GFP conjugate, indicated a decoration yield of ~8 ± 2 Fc-PEG chains per GFLV (Supplementary Material). Proper functionalization of surface-adsorbed GFLV by GDH-Nb_{75} and the redox Nb_{59}-GFP-Fc-PEG are evidenced below.

3.2 Characterizing the Nb-driven assembly of PQQ-GDH on GFLV

After being exposed to GDH-Nb_{75} (step (3) in Figure 1), gold surfaces bearing the GFLV nanoarray were mounted as the working electrode in a standard three-electrode electrochemical fluid-cell filled with 50 mM pH = 7.5 Tris-HCl buffer. Cyclic voltammograms were then recorded, by scanning the electrode potential, *E,* from + 0 to + 0.35 V/SCE and back, while ferrocenedimethanol (Fc) and glucose (G) were sequentially added to the cell, Figure 2A. A very low (3 µM) concentration of ferrocenedimethanol was initially selected, as it is known that the enzymatic activity of electrode-immobilized PQQ-GDH is easier to evidence in this case (i.e. with less interference from glucose depletion).[66] The CV recorded in the absence of glucose, $i_0(E)$, is the sum of the current due to the diffusion of Fc, and of the capacitive background signal of the electrode (Figure 2A, red trace). After correction from the capacitive signal, recorded in a solution containing only the buffer, the diffusive CV of Fc was obtained (Inset in Figure 2A). It displayed the expected pair of current peaks, centered around the standard potential of ferrocenedimethanol ($E°$ = 0.230 V/SCE),[67] and separated by ~ 60 mV. These characteristics are typical of a species undergoing rapid electron transfer with the gold electrode.

Upon addition of glucose to the solution, the current greatly increased in intensity and developed a well-defined S-shape (blue trace in, Figure 2A). Such a behavior evidences the occurrence of an electro-

catalytic cycle at the electrode, where the oxidized form of ferrocenedimethanol, ferrocenium (Fc^+), produced upon scanning the electrode potential anodically, is used as a co-substrate by the virion-bound GDH molecules for oxidizing glucose into gluconolactone (GL), Figure 2B. The observation of a S-shaped signal ensures that the current solely reflects the enzymatic activity, without interference from diffusion of the co-substrate.[68] We verified that, in the absence of ferrocenedimethanol on solution, no catalytic current was recorded, evidencing that Fc^+ was required to convey the electrons from the electrode to the PQQ-GDH enzyme (Figure S5).

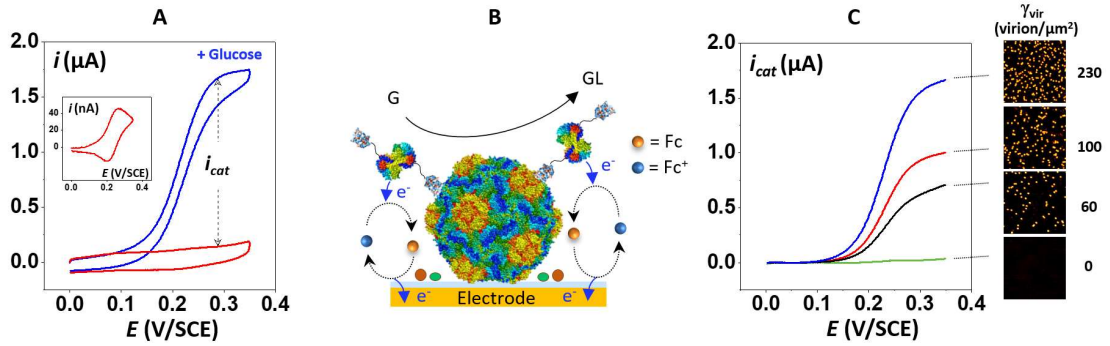

Figure 2. (A) Cyclic voltammograms (CVs) recorded at a TS gold electrode bearing GFLV decorated by the GDH-Nb_{75} fusion, in the presence of 3 µM ferrocenedimethanol (Fc), both before (red trace) and after (blue trace) injection of glucose (G) up to a concentration of 3 mM. The inset shows the CV recorded before glucose correction, corrected from the capacitive background current. (B) Schematics of the decorated particles and of the catalytic cycle triggered by glucose injection: the enzyme converts glucose into gluconolactone (GL) using the electrode-produced oxidized form of ferrocenedimethanol (Fc^+) as a redox co-substrate. (C): CVs recorded in the presence of 3µM Fc and 3 mM glucose at a TS gold electrode bearing GDH-Nb_{75}-decorated GFLV at various surface coverage, γ_{vir}, as indicated. Virus coverages were determined by counting virions from AFM-images, as shown. 50 mM pH = 7.5 Tris-HCl buffer. Potential scan rate = 20 mV/s. T = 25 °C.

The intensity of the catalytic plateau current, $i_{cat,pl,}$ defined as the intensity of the plateau current of the voltammogram, i_{pl}, corrected from the small current recorded in the absence of glucose, was observed to increase when increasing the coverage of decorated virus on the surface (Figure 2C). More precisely, a linear relationship of $i_{cat,pl}$ with γ_{vir}, was obtained, which displayed a very small intercept value (Figure 3A). This result ascertains that the GDH-Nb_{75} was functional and properly immobilized on the surface-adsorbed GFLV particles, with a negligible level of non-specific adsorption of the fusion protein on the electrode surface. Importantly, only a modest ~20 % decrease of the catalytic plateau current was recorded upon storing the electrodes at 4°C for a week in Tris Buffer, showing the good global stability and functionality of the nano-assembly on the surface.

In order to assay the average number of GDH molecules per virion, several gold surfaces bearing decorated GFLV particles at various coverages were submitted to a multi-step chemical treatment, designed to strip-off the PQQ prosthetic group from the GDH molecules present on the surface (Supplementary Material). The amount of PQQ thus recovered was then precisely measured using a highly sensitive enzymatic assay (Supplementary Material).[66,69,70] This yielded the amount of GDH molecules initially present on the surface, taking into account that PQQ-GDH incorporates two PQQ moieties per enzyme. For each electrode considered, this enabled us to plot the amount of GDH molecules, expressed as molecules per unit surface area (γ_{GDH}), as a function of the virion coverage on the surface, a linear variation was observed (Figure 3B).

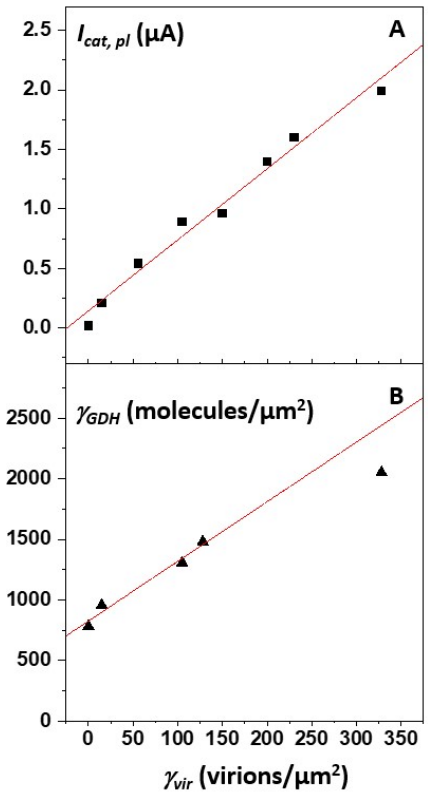

Figure 3. Dependence on the surface coverage of GDH-Nb_{75}-decorated GFLV particles, γ_{vir}, of : (A) The intensity of the catalytic plateau current, $i_{cat,pl}$, measured in a buffer solution containing 3 µM Fc and 3 mM glucose. (B) Amount of GDH stripped from the surfaces, expressed as a GDH molecules per unit surface area, γ_{GDH}.

The average number of GDH molecules immobilized per virion was given by the slope of this plot, yielding 5 ± 1 GDH per virion. This number is rather low considering 60 Nb_{75} epitopes are present on each GFLV particle.[62] Such a result is in part a consequence of the immobilization of the virions at the gold surface and further blocking step that inevitably prevent access of GDH-Nb_{75} to the hidden epitopes (*i.e.* those engaged in GFLV-cysteamine-activated gold surface interactions). It is also possible that the immobilization steps may lead to partial denaturation of the virions, resulting in loss of GDH-Nb_{75} binding. It also cannot be excluded that GDH-Nb_{75} may have reduced ability to bind to GFLV compared to native/unfused Nb_{75}. Formation of the Nb_{75}-GFLV immunocomplex requires that the N-terminus of the nanobody is oriented towards the virus capsid,[62] which may have been partly impaired here by the presence of GDH at this terminus. If so, this effect could be possibly alleviated by further increasing the length of the linker separating the two proteins in the fusion.

We also note from Figure 3B, that the linear relationship between γ_{GDH} and γ_{vir} is characterized by a non-zero intercept, which may either indicate a systematic measurement offset or the presence of traces of contaminant PQQ in the samples, or of PQQ-containing GDH molecules non-specifically adsorbed on the surface. In the latter case scenario, adsorbed GDH molecules were necessarily catalytically inactive, since no catalysis was recorded in the absence of virus (Figure 3A). The presence of non-active adsorbed GDH molecules on the surface would be of no importance for the rest of the study.

3.3 Kinetic characterization of the GFLV-supported PQQ-GDH

We conducted a thorough kinetic characterization of the enzymatic activity of the virus-attached PQQ-GDH, by recording the electrocatalytic response of gold surfaces bearing GDH-decorated GFLV particles, in the presence of ferrocene dimethanol, for a wide range of glucose concentrations. Figure 4

presents sets of catalytic CVs recorded at two of such surfaces, either in the presence of a low (3 µM, Panel I) or a high (300 µM, Panel II) ferrocenedimethanol bulk concentration, $[Fc]_b$. These largely differing concentrations were chosen so as to be respectively sufficiently low and high enough to *a priori* allow the observation of the two limiting catalytic regimes of PQQ-GDH.[71] At low mediator concentration this enzyme is known to behave non-cooperatively, that is each of its two subunits function independently. At high mediator concentration, the enzyme functions cooperatively, i.e. the binding of a glucose molecule to the active site of one subunit enhances the activity of the other. [71]

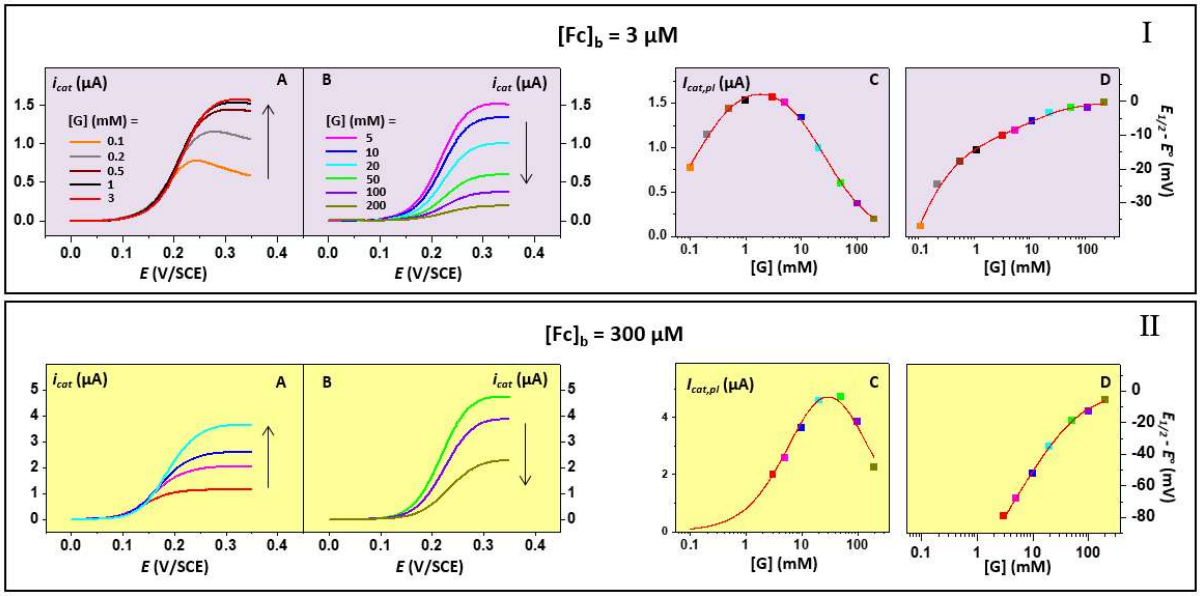

Figure 4. Cyclic voltammetry response of TS gold electrodes bearing arrays of GDH-Nb_{75}-decorated GFLV particles. Panel I - (A, B): Catalytic voltammograms, i_{cat} vs. E, recorded in the presence of 3 µM ferrocenedimethanol (Fc), for various glucose concentrations, [G], as indicated. (C): Dependence of the catalytic plateau current $i_{cat,pl}$ as a function of [G]. (D): Variation of the potential at mid-height of the catalytic CV as a function of [G]. γ_{vir} = 280 virions/ µm^2. Panel II- Data similar to those in Panel I but acquired at a different electrode and for a higher Fc concentration of [Fc] = 300 µM. γ_{vir} = 40 virions/ µm^2. 50 mM pH = 7.5 Tris-HCl buffer. Potential scan rate = 20 mV/s. T = 25 °C.

In Figure 4A, Panel I, it can be seen that, for the low ferrocenedimethanol concentration case, the intensity of the catalytic CV increased rapidly as the glucose concentration, [G], was raised from 0.1 mM to 3 mM. For [G] = 0.1 mM and 0.2 mM the CV displayed a broad peak, rather than a plateau, due to glucose being partly depleted (e.g., significantly consumed by the enzyme) at the electrode surface in the time frame of the CV. Yet, the expected S shape could be observed for [G]= 0.5 mM and above. For [G] > 3 mM, the plateau current decreased after each glucose addition, reflecting the known substrate inhibition of PQQ-GDH (Figure 4B, Panel I).

For the high ferrocenedimethanol concentration case, the plateau current of the catalytic CV was observed to increase with [G], up to a concentration of [G] ~20 mM, after what it decreased upon further glucose addition (Figure 4A and 4B, Panel II). Note that due to the high activity of PQQ-GDH when in its cooperative mode, a relatively low virus coverage of γ_{vir} = 40 virions/ µm^2 had to be used in that case to avoid glucose depletion by the rapid enzymatic reaction.

Analysis of the dependence of the CV signals shown in Figure 4 on the glucose concentration can yield quantitative information regarding the kinetics of the GFLV-supported enzyme. Several observables can be chosen for this analysis, the most straightforward being the intensity of the catalytic plateau current $i_{cat,pl}$. The dependence of $i_{cat,pl}$ as a function of the glucose concentration, both for $[Fc]_b$= 3 µM and $[Fc]_b$ = 300 µM, is shown in Figure 4C, Panel I and II, respectively.

The plots reveal that the variation of $i_{cat,pl}$ vs. [G] follows a bell-shaped pattern, which is typical of an enzyme that is inhibited by its substrate. However, it is also evident that the peak of this pattern is located in different glucose concentration regions depending on the concentration of ferrocedimethanol. Inhibition is seen to occur at a lower glucose concertation for $[Fc]_b$ = 3 µM than for $[Fc]_b$ = 300 µM. The peak width is also wider in the former case versus the latter. These characteristics are qualitatively similar to those typical of the electrocatalytic response of PQQ-GDH in solution.[71]

In order to extract quantitative information regarding the enzyme kinetics, one needs to recall that, in a configuration where the enzyme is immobilized on an electrode surface, and interrogated using a soluble co-substrate (mediator), the catalytic current is simply proportional to the enzymatic rate,[68] so that here:[66]

$$i_{cat} = 2Fn_{GDH}/\left[\frac{1}{k_{ox}\,[Fc^+]_{ez}}(1 + K_i[G]) + \frac{1}{k_{cat}} + \frac{K_M}{k_{cat}[G]}\right] \quad (1)$$

where F is the Faraday constant. $n_{GDH} = S\gamma_{GDH}$ is the molar amount of enzyme interrogated, S being the electrode surface area. $[Fc^+]_{ez}$ is the Fc^+ concentration as seen by the enzyme. Due to fast diffusion of Fc^+ across the virus length-scale, $[Fc^+]_{ez}$ equals $[Fc^+]_e$, the Fc^+ concentration at the electrode surface. [G] is the bulk glucose concentration. k_{cat} is the catalytic constant of the enzyme, K_M the Michaelis constant for glucose, k_{ox} the second-order rate constant corresponding to the oxidation of the enzyme by Fc^+ and K_i the equilibrium constant of the enzyme inhibition by glucose.

This kinetic equation was previously shown to be valid in both of the cooperative and non-cooperative mode of PQQ-GDH, differing only by the value of the individual kinetic constants.[66,71] Considering that at the plateau current, the concentration of the ferrocenium species produced at the electrode equals the bulk concentration of ferrocedimethanol, i.e. $[Fc^+]_e = [Fc]_b$, Equation (1) can a priori be fitted to the experimental $i_{cat,pl}$ vs. [G] data presented in Figure 4C in both Panels. Such a fitting allows to reproduce the bell-shape of the experimental curves (red traces), based on 4 fitting parameters, namely k_{ox}, k_{cat}, K_M, K_i, while n_{GDH} is independently known. This provides a qualitative indication that PQQ-GDH present on functionalized GFLV follows the same kinetic scheme as in solution. However, because the number of fitting parameters is too high, several sets of (k_{ox}, k_{cat}, K_M, K_i) values could reproduce equally well the data. It is thus not possible to obtain the individual values of those kinetic constants by analyzing the $i_{cat,pl}$ vs. glucose variation. We therefore turned to another observable, never so far considered for analyzing PQQ-GDH kinetics, that is the potential at mid-height of the catalytic wave, $E_{1/2}$. This observable also displayed a sharp dependence on glucose concentration, both for low and high Fc concentration (Figure 4D, Panels I and II). Analyzing this variation requires that the kinetic Equation (1) is explicitly related to the electrode potential, E. This is made possible by the fact that ferrocendimethanol is a redox species rapidly and reversibly exchanging single electrons with metal electrodes, so that the concentration of Fc^+ at the electrode is simply related to the electrode potential by Nernst Law:

$$[Fc^+]_e = [Fc]_b/(1 + \exp[-F(E - E^0)/RT]) \quad (2)$$

Hence the theoretical expression of $E_{1/2}$ can be derived from Equation (1):

$$E_{1/2} = E^0 - \frac{RT}{F} ln\{1 + k_{ox}[Fc]_b(1 + K_M/[G])/[k_{cat}(1 + K_i[G])]\} \quad (3)$$

This expression allowed the experimental $E_{1/2}$ vs. [G] variations to be nicely reproduced, using only 3 adjustable parameters, namely (k_{ox} / k_{cat}), K_M, and K_i, both for low and high Fc concentrations, red traces (Figure 4D, both Panels). Note that, besides a reduction in the number of parameters, the potential interest of considering $E_{1/2}$ rather than $i_{cat,pl}$ for analyzing the kinetic response of PQQ-GDH is that fitting does not require the enzyme coverage to be known. The sets of best-fit values we thus obtained are collected in columns I and III of Table 1, for the low and high Fc concentrations, respectively. They are to be compared with data presented in Columns V and VI, which correspond to the kinetic behavior of PQQ-GDH in solution, in the non-cooperative and cooperative mode, respectively.

	GFLV-supported PQQ-GDH Fc co-substrate in solution				PQQ-GDH in solution Fc co-substrate in solution		GFLV-supported PQQ-GDH + PEG-Fc *integrated system*	
	$[Fc]_b$ = 3µM		$[Fc]_b$ = 300 µM		Non-cooperative	Cooperative		
	$E_{1/2}$ analysis	Full analysis	$E_{1/2}$ analysis	Full analysis	Literature values, reference [66]		$E_{1/2}$ analysis	Full analysis
K_M (mM)	0.45 ± 0.2	0.35 ± 0.15	50 ± 20	10 ± 2	0.27 ± 0.05	4.7 ± 0.3	1.5 ± 0.6	4.4 ± 1.5
K_i (M^{-1})	127 ± 55	60 ± 50	30 ± 15	50 ± 15	52 ± 6	127 ± 20	65 ± 55	9. 7± 2.4
k_{ox} / k_{cat} (M^{-1})	1.9 ± 0.7 × 10^5	3.0 ± 1.0 × 10^5	0.4 ± 0.2 × 10^4	1.2 ± 0.4 × 10^4	1.3 ± 0.45 × 10^5	5.5 ± 0.45 × 10^4	N.A	N.A.
$k_{ox}[Fc]_{ez}/k_{cat}$	N.A.	N.A.	N.A.	N.A	N.A.	N.A.	0.80 ± 0.24	1.0 ± 0.2
k_{ox} ($M^{-1}s^{-1}$)	N.A.	2.4 ± 1.0 × 10^8	N.A.	2.4 ± 1.3 × 10^8	1.9 ± 0.3 × 10^8	3.3 ± 0.6 × 10^8	N.A.	N.A.
k_{cat} (s^{-1})	N.A.	0.8 ± 0.3 × 10^3	N.A.	2 ± 1 × 10^4	1.5 ± 0.3 × 10^3	6 ± 1 × 10^3	N.A.	4 ± 1 × 10^3
	I	II	III	IV	V	VI	VII	VIII

Table 1. Kinetic constants of PQQ-GDH in its cooperative and non-cooperative kinetic modes and in the various configurations indicated. Error margins correspond to the dispersion of the values of the constants derived from two series of experiments analyzed by two different experimentalists.

Comparing the values presented in Columns I and V, once can see that the $E_{1/2}$ analysis at low Fc concentration yielded a K_M value that was in good agreement with the typically low value reported for the non-cooperative mode of PQQ-GDH. On the other hand, the K_i value was 2-3 times higher than the corresponding literature value measured in solution. However, the comparison of these values is less meaningful due to the large error margin in our K_i measurement from $E_{1/2}$ analysis. In contrast, the value we obtained for the k_{ox} / k_{cat} ratio, closely agreed with the value typical of the non-cooperative mode of PQQ-GDH in solution.

The values of the kinetic constant measured from the $E_{1/2}$ analysis at high Fc concentration (Column III) are clearly distinct from those measured at low concentration. In particular, the value of K_M is significantly higher, and that of the k_{ox}/k_{cat} ratio lower, at high than at low Fc concentration. The values obtained in the former tend toward those typical of the cooperative mode (Column VI) without reaching them completely, perhaps because of a still insufficient Fc concentration.

At this point, we have shown that the easy and immediate measurement of the half-wave potential of the catalytic signal allows a rapid comparison between the typical kinetic parameters of PQQ-GDH either in solution or carried by GFLV. Our findings seem to indicate that the kinetics of this enzyme are not positively or negatively affected by mere scaffolding, at least when a soluble redox mediator is used.

Complete analysis of the kinetic behavior of PQQ-GDH requires that the *individual* values of the most important kinetic constants k_{ox} and k_{cat} are determined, which cannot be achieved from $E_{1/2}$ measurements. We therefore turned toward a more complete data treatment, that we had introduced earlier,[68] and which consists in analyzing the catalytic wave in its entirety. This method relies on the fact

that the co-substrate concentration sensed by the surface-confined enzyme, i.e., the Fc^+ concentration at the electrode, varies continuously all along the CV as it is related to the electrode potential by Nernst law, Equation (2). As a result, the co-substrate dependence of the enzyme kinetics is fully captured by the variation of the catalytic current versus the electrode potential.

Rewriting Equation (1) as the reciprocal of the catalytic current one obtains:

$$\frac{1}{i_{cat}} = \frac{1}{2Fn_{GDH}}\left[\frac{1+K_i[G]}{k_{ox}\,[Fc^+]_e} + \frac{1}{k_{cat}}\left(1+\frac{K_M}{[G]}\right)\right] \qquad (4)$$

$[Fc^+]_e$ can be calculated from Nernst law for any point along the catalytic voltammograms, knowing the electrode potential. This enables the catalytic voltammograms presented in Figure 4, recorded at various glucose concentrations, to be replotted in a $1/i_{cat}$ vs. $[Fc^+]_e$ format in Figure 5A, Panel I and II for $[Fc]_b$= 3 µM and 300 µM, respectively.

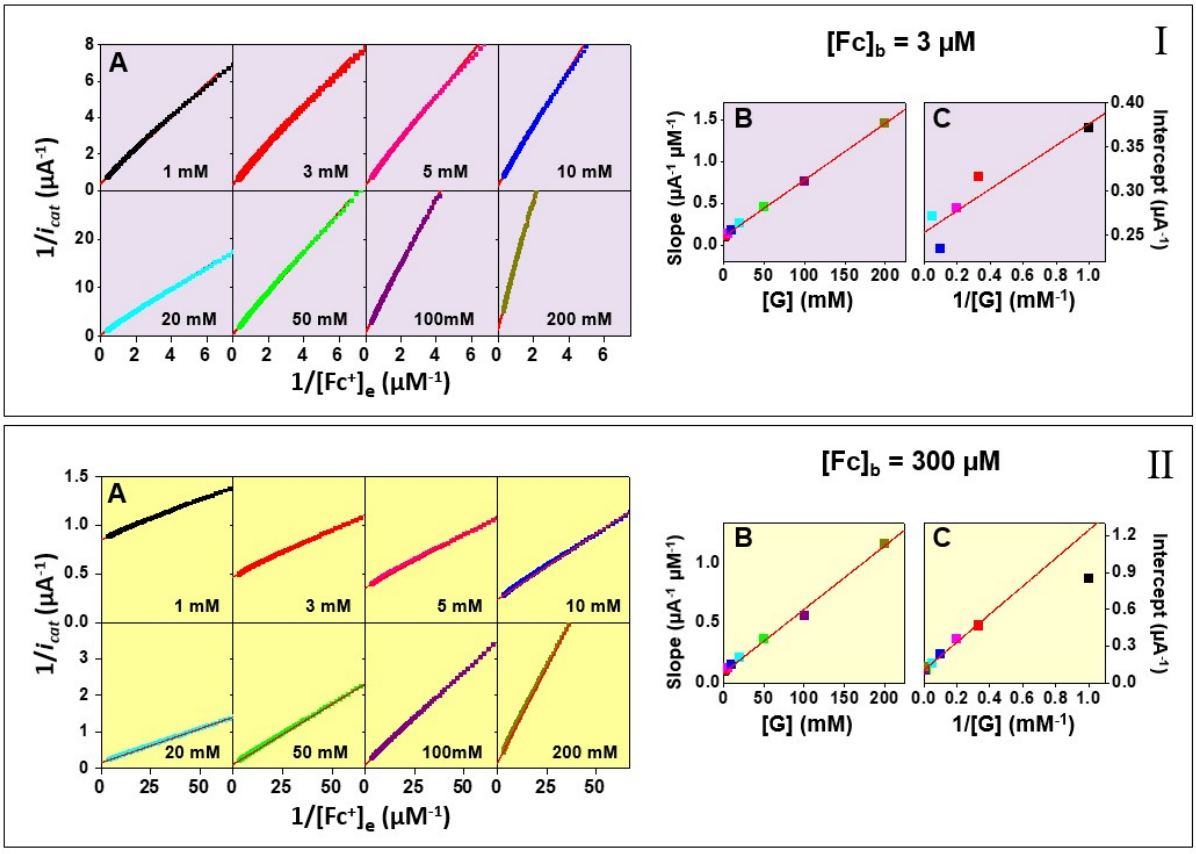

Figure 5. Full kinetic analysis of the electrochemical response of PQQ-GDH-functionalized GFLV particles adsorbed on gold surfaces, using ferrocenedimethanol, Fc, as a soluble co-substrate. In Panels I and II, ferrocenedimethanol concentrations are $[Fc]_b$ = 3 µM and 300 µM, respectively. Various glucose concentrations, [G], ranging from 1 - 200 mM are considered as explicitly indicated. (A): Reciprocal "primary" plots of the catalytic current, i_{cat}, as a function of the reciprocal of the co-substrate concentration at the electrode, $[Fc^+]_e$, as calculated from Nernst equation. (B): Slope of the primary plots as a function of [G]. (C) Intercept of the primary plots vs. the reciprocal of [G].

As predicted by Equation 4, a linear variation of $1/i_{cat}$ vs. $[Fc^+]_e$ was obtained for such "primary" plots, validating our method of analysis. The theoretical expressions of the slope, s_1, and intercept, o_1, of the lines are given by:

$$s_1 = \frac{1}{2Fn_{GDH}}\left[\frac{1+K_i[G]}{k_{ox}}\right] \quad (5)$$

$$o_1 = \frac{1}{2Fn_{GDH}}\left[\frac{1}{k_{cat}}\left(1+\frac{K_M}{[G]}\right)\right] \quad (6)$$

As anticipated from the above equations, the slopes of the experimental $1/i_{cat}$ vs. $[Fc^+]_e$ plots are seen to increase, and their intercept to decrease, with increasing glucose concentration (Figure 5A, Panels I and II). Experimental s_1 and o_1 values were respectively plotted as a function of [G] and 1/[G] in "secondary plots" reproduced in Figures 5B and 5C, Panels I and II. In each case the linear variations described by Equations (5) and (6) were observed. The slope and the intercept of the s_1 vs. [G] plots yielded the values of $\frac{1}{2Fn_{GDH}}\left[\frac{K_i}{k_{ox}}\right]$ and $\frac{1}{2Fn_{GDH}}\left[\frac{1}{k_{ox}}\right]$, respectively, from which the K_i value could be immediately obtained. Similarly, the slope and the intercept of the o_1 vs. 1/[G] plots yielded the values of $\frac{1}{2Fn_{GDH}}\left[\frac{K_M}{k_{cat}}\right]$ and $\frac{1}{2Fn_{GDH}}\left[\frac{1}{k_{cat}}\right]$, from which the value of K_M was derived. With the K_i and K_M values in hand, the individual values for k_{ox} and k_{cat} could then be obtained from the slopes of the secondary plots. This required that n_{GDH} was first estimated from the virus coverage and the average number of 5 GDH molecules per GFLV. Overall, the whole-CV analysis method, albeit seemingly complex, had the advantage of allowing the determination of the individual values of all of the kinetic constants of the GFLV-bound PQQ-GDH. These values are reported in Columns II and IV of Table 1, for the low and high Fc concentration case, respectively. Their availability uniquely enables searching for any effect of scaffolding on catalysis.

Comparing the data presented in Columns II and V, it appears that all of the kinetic constants characterizing the action of PQQ-GDH at low Fc concentration are very close to those typical of the non-cooperative mode of this enzyme in solution.

The individual kinetic constants recorded at high Fc concentration for the GFLV-scaffolded PQQ-GDH (Column IV) are also close to their counterparts typical of the cooperative regime (Column VI), albeit the agreement is not quite as good as observed for the low Fc concentration case. In particular, the k_{cat} value recorded for the GFLV-scaffolded GDH appears ~3 times higher than for the enzyme in solution. However, since the K_M and K_i values appear respectively twice higher and lower (double and half) than the reference solution values, it seems reasonable to conclude that, overall, within experimental uncertainties the rate constants measured for PQQ-GDH either GFLV- displayed and free in solution are the same. This brings the definitive proof that Nb-guided scaffolding of PQQ-GDH on GFLV did not modify the kinetic scheme of this enzymes, nor altered (decreased or enhanced) its catalytic activity. Hence, in spite of the highly confined and charged environment experienced by the enzyme when on the GFLV scaffold no kinetic effect was observed. This result suffices to prove that the small size and high electric charge of viral nano-scaffolds do not universally modulate the activity of redox enzymes, and certainly not of PQQ-GDH.

The above detailed kinetic study was also an indispensable prerequisite for the next step of our study, as it now allows us to investigate specifically the kinetic effect of replacing a soluble redox co-substrate by one confined to GFLV particles on PQQ-GDH activity.

3.4 Nanobody-driven assembly of the Fc-PEG integrated system on GFLV

The electrodes carrying GDH-decorated GFLV particles were exposed to Fc-PEGylated Nb_{59}-GFP, and characterized using square wave cyclic voltammetry (SWV). The resulting signals showed a broad peak, located at a potential close to the standard potential of the Fc heads of the PEG chains ($E° \sim 0.15$ V/SCE), Figure 6A, red trace. Importantly no such peak was seen when a BSA/B2-GFP blocked electrode, not carrying virus particles, was exposed to the Fc-PEG-Nb_{59}-GFP (Figure 6A, dashed black trace).

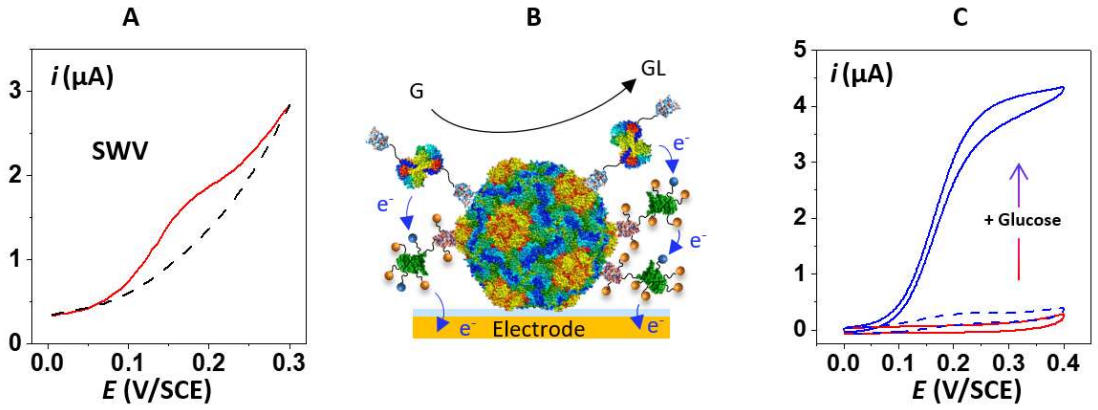

Figure 6. Electrochemical and electro-catalytic response of the Fc-PEG/PQQ-GDH integrated system assembled on GFLV particles using nanobodies. (A) Square Wave Voltammetry signal recorded at an electrode bearing GFLV decorated with Fc-PEGylated Nb_{59}-GFP and GDH-Nb_{75}, recorded in buffer (no glucose), red trace. The dotted black trace was recorded at a BSA/B2-GFP blocked electrode, not carrying GFLV, which was exposed to both nanobodies. SWV parameters: amplitude 25 mV, frequency 25 Hz, increment 5 mV. (B) Schematics of the PQQ-GDH catalyzed glucose oxidation mediated by Fc-PEG, occurring on decorated GFLV particles. (C) Catalytic voltammogram recorded at an electrode bearing GFLV decorated by both Fc-PEGylated Nb_{59}-GFP and GDH-Nb_{75}, recorded before (red trace) and after (blue trace) injection of glucose in the cell, up to a 20 mM concentration. The blue dotted trace was recorded in the latter conditions, at a BSA blocked electrode, not carrying GFLV, which was exposed to both nanobodies. Scan rate = 20 mV/s.

These results indicate that Fc-PEG chains were selectively immobilized on the virus, via the immunological assembly of the Fc-PEG-nanobody (Figure 6B). The number of Fc-PEG chains present on the surface, and ultimately per GFLV particle, is hard to estimate from the SWV signal, which does not depend on this parameter in an analytically simple way. We thus turned to cyclic voltammetry, which is a more quantitative electrochemical technique, to characterize the response of Fc-PEG decorated GFLV. However, the CV signals (Figure S6) were found to be dominated by the capacitive response of the electrode, which was, by design, suppressed in SWV. Capacitive background correction was nevertheless possible, yielding to an estimation of the surface coverage in Fc-PEG in the ~ 2 pmol/cm^2 range. Knowing the GFLV coverage on the electrodes, this value can be converted into a number of Fc-PEG chains per GFLV of ~56. Considering 8 Fc-PEG chains per Fc-PEGylated Nb_{59}-GFP were present, we could finally estimate an average of 7 ± 2 redox-labeled Nbs were decorating each GFLV particle. This number appears quite low considering the theoretical presence of 60 Nb_{59} epitopes per particle. Such a result can be explained in part by the bulkiness of the Fc-PEG chain which limits the recognition of the GFLV by Fc-PEG- Nb_{59}-GFP and the inaccessibility of the epitopes involved in electrode adhesion.

3.5. Catalytic activity of the Fc-PEG/PQQ-GDH integrated system on GFLV

Upon introducing glucose in the buffer solution bathing the gold surface bearing GFLV decorated by both the GDH-Nb_{75} and Fc-PEG-Nb_{59}-GFP, the CV increased strongly in intensity and acquired the typical S-shape of catalytic signals (Figure 6C, blue solid line). Such an obvious change evidences that,

as depicted in Figure 6B, the oxidized ferrocene heads effectively play the role of a redox co-substrate for the virus-supported PQQ-GDH molecules, and convey the electrons released by glucose oxidation to the electrode. Such an electron transport process involves random Brownian motion of the Fc-PEG chain, coupled to electron exchange between transiently neighboring Fc heads.[49,72] Note that, in the absence of viral particle on the surface, only a very small catalytic signal was detected (Figure 6C, dotted line). This signal is due the negligibly small amount of GDH-Nb_{75} and Fc-PEG-Nb_{59}-GFP non-specifically adsorbed on the electrode, which is hardly detectable in the absence of catalysis.

Having demonstrated the effective assembly and activity of the Fc-PEG/PQQ GDH integrated system on GFLV virions, we were able to proceed with the search for kinetic effects of scaffolding.

3.6. Kinetic characterization of the Fc-PEG/PQQ-GDH integrated system scaffolded on GFLV

Evolution of the catalytic voltammograms, $i_{cat}(E)$ recorded at an electrode bearing GFLV particles decorated by the Fc-PEG/PQQ-GDH integrated system, as a function of glucose injection in the electrochemical cell, is displayed in Figure 7A and 7B, Panel I.

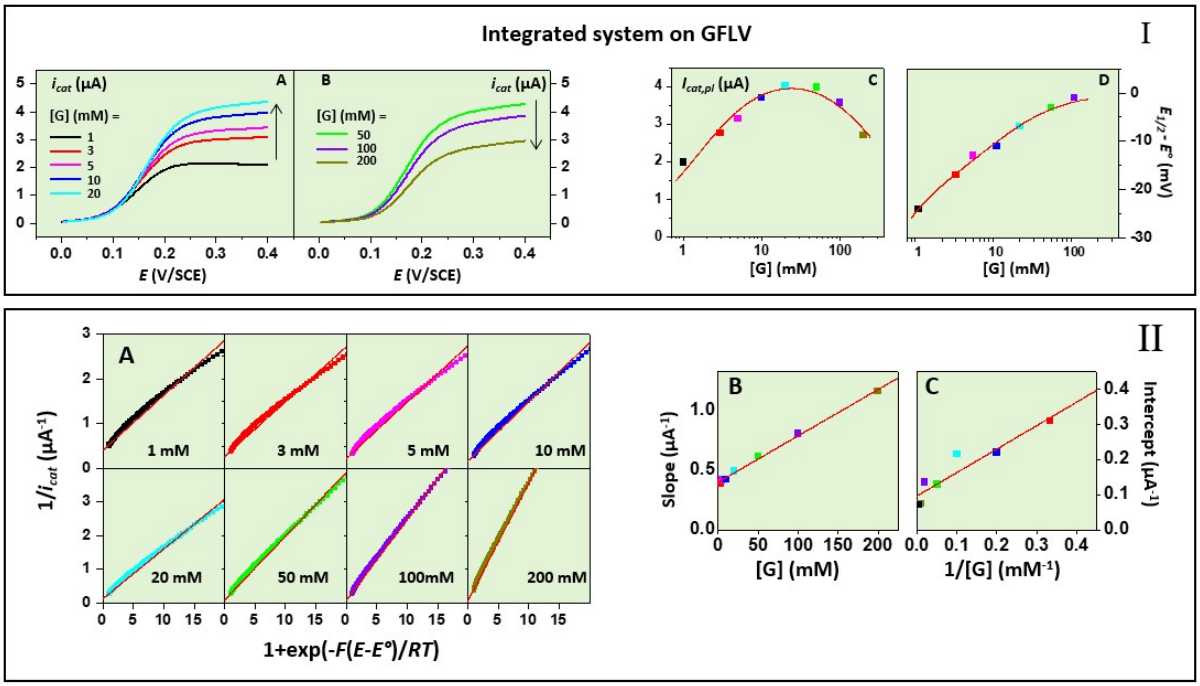

Figure 7. Kinetic characterization of the Fc-PEG/PQQ-GDH integrated system assembled on GFLV particles. Panel (I): (A), (B): Catalytic CVs recorded at a gold electrode bearing the functionalized/integrated GFLV system for the various glucose concentrations indicated. (C), (D): Variations of the catalytic plateau current, $i_{cat,pl}$ and of the mid-height potential, $E_{1/2}$, of the catalytic CVs, respectively. Panel II: (A): Primary plots showing the reciprocal of the catalytic current, $i_{cat}(E)$ as a function of the term $1+\exp(F(E-E°)/RT)$, for the glucose concentrations indicated. (B): Slope of the primary plots as a function of the glucose concentrations, [G]. (C): Intercept of the primary plots as a function of the reciprocal of the glucose concentrations.

One can observe that the intensity of the catalytic plateau current, $i_{cat,pl}$ increased as the glucose concentration was raised up to ~20 mM and decreased upon further glucose addition. Consequently, a bell-shaped i_{cat} vs. [G] plot was obtained, Figure 7C, Panel I. Equation (1) enables to model this variation, using $k_{ox}[Fc^+]_{ez}$, k_{cat}, K_M, K_i using as adjustable parameters, showing qualitatively that PQQ-GDH-catalyzed glucose oxidation in the integrated system follows the same kinetic scheme as in solution. However, as explained above such a fit cannot yield individual values of the kinetic constants.

The dependence of the potential at mid-height of the catalytic waves on the glucose concentration can provide more information. Yet, unlike when a soluble ferrocene mediator is used the Fc^+ concentration as seen by the enzyme, $[Fc^+]_{ez}$, is not straightforwardly know, as it depends on the complex electron transport mechanism of Fc^+ along GFLV particles (Figure 6B). Yet, assuming a Nernstian electron transfer at the electrode, one can write:

$$[Fc^+]_{ez} = [Fc]_{ez}/(1 + \exp[-F(E - E^0)/RT]) \quad (7)$$

Where $E°$ is the standard potential of the Fc head. $[Fc]_{ez}$ is the concentration of Fc head in the vicinity of the enzyme at equilibrium (when no current flows). The value of $[Fc]_{ez}$ is difficult to evaluate as it requires to make assumptions regarding the exact spatial arrangement of the Fc-PEG chains around GFLV.[49,72]

Nevertheless, Equation (3) can still be used to fit the $E_{1/2}$ vs. [G] data, simply replacing $[Fc]_b$ by $[Fc]_{ez}$, and using K_M, K_i and the ratio $k_{ox}[Fc]_{ez}/k_{cat}$ as adjustable parameters. A good adjustment of the calculated curve on the experimental data points is obtained, Figure 7D, Panel I, yielding the best fit values gathered in Table 1, Column VII. The value thus estimated for K_M and K_i lie between those typical of the cooperative and non-cooperative regime of PQQ-GDH, so that no conclusion can be drawn from these parameters regarding the regime adopted by the GFLV-supported PQQ-GDH. This emphasizes the need for the complete determination of the individual kinetic constants, that only a detailed analysis of the whole catalytic CV wave can provide. This first requires slightly rearranging Equation (1), to take into account the definition of $[Fc+]_{ez}$ for the integrated system (Equation(7)), yielding:

$$\frac{1}{i_{cat}} = \frac{1}{2Fn_{GDH}}\left[\frac{1+K_i[G]}{k_{ox}\,[Fc]_{ez}}(1 + \exp[-F(E - E^0)/RT]) + \frac{1}{k_{cat}}\left(1 + \frac{K_M}{[G]}\right)\right] \quad (8)$$

As suggested by this expression the reciprocal of the catalytic current $1/i_{cat}(E)$, measured all along the catalytic voltammograms, was plotted as function of the term $1 + \exp[-F(E - E^0)/RT]$. The resulting experimental plots, constructed for various glucose concentrations, are shown in Panel II, Figure 7A. They are observed to be linear, as predicted by equation (8), validating our analysis qualitatively. As expected, their slope is seen to increase and their intercept to decrease, with increasing glucose concentration. The slope, s_1, and origin, o_1, of these primary plots are plotted versus the glucose concentration, or its reciprocal, in Panel II, Figure 7A and 7C, respectively. In both cases, linear variations are obtained, as predicted by Equations (5) and (6). The ratio of the slope over the intercept of each of these two secondary plots immediately yields K_i and K_M values, respectively. The ratio of the respective slopes of the two secondary plots yields the value of the global parameter $k_{ox}[Fc]_{ez}/k_{cat}$. Finally, considering $n_{GDH} = 5$ enables the value of k_{cat} to be estimated from the intercept of the o_1 vs 1/[G] variation. The individual values thus obtained for the kinetic constants characterizing the activity of PQQ-GDH in the integrated system supported by GFLV are collected in Column VIII of Table 1.

One can first notice that the K_M value for the GFLV-supported system is very close to that typical of the cooperative mode of PQQ-GDH in solution (Column VII vs. Column VI). The k_{cat} value is clearly larger than expected for the non-cooperative mode, being close, albeit slightly smaller, than that of the cooperative mode. These observations strongly suggest that PQQ-GDH in the GFLV-scaffolded integrated system adopts its most effective cooperative kinetic regime. Importantly this behavior is not due to mere attachment of the enzyme to GFLV particles, since we observed hereabove that the kinetic behavior of PQQ-GDH was not modified by its positioning on the GFLV capsid. We conclude therefore that the cooperative regime adopted by PQQ-GDH in the GFLV-supported integrated system is due to the nanoscale confinement of the Fc heads in the vicinity of the enzyme.

The origin of this clear example of modulation of the enzymatic activity by nanoscaffolding can be understood by considering the specificity of cooperativity for a redox enzyme such as PQQ-GDH: confinement of the ferrocene co-substrate around the enzyme increases the probability that both catalytic units of GDH are simultaneously in the same (oxidized) redox state, which is a necessary condition for their cooperative action toward glucose. Of note, we observed a similar phenomenon when the Fc-PEG/GDH integrated system was scaffolded on flexuous *fd*-bacteriophage or rod-like TMV particles, but not when it was directly assembled on planar electrodes.[49] This evidences that enzymatic enhancement is specifically due to confinement of the system on viral particles displaying (at least one) dimension in the ~10 nm range. The exact shape of the particle seems to have little importance in that respect.

Considering Table 1 again, one can observe that the K_i value obtained for the GFLV-scaffolded integrated system is significantly smaller than that corresponding to both the non-cooperative and cooperative mode of GDH. We previously observed the same effect for the Fc-PEG/GDH integrated system, either scaffolded on viruses or assembled as a monolayer on electrodes, but not for virus-bound GDH using a soluble mediator. Hence, it can be concluded that substrate inhibition is minimized as a benefit of the co-immobilization of the mediator and the enzyme, and not of nano-scaffolding.

4. Conclusion

We have developed an original protocol to topologically control the assembly of GDH-based enzymatic systems on the capsid of icosahedral GFLV particles immobilized on electrode surfaces. This was made possible by using nanobodies specifically targeting structurally well-defined areas at the viral nanoparticle surface. This configuration allows for a simple and thorough analysis of the kinetic response of virus-particle scaffolded enzymatic systems through cyclic voltammetry. By selecting appropriate observables, individual kinetic constants of the enzyme can be determined. This methodology was employed to investigate kinetic effects of nano-scaffolding on the activity of PQQ-GDH. Results indicate that immobilization of the enzyme on viral particles alone does not enhance enzymatic activity despite the small size (~30 nm) and charged nature of the GFLV particles, two parameters usually thought to promote such effect. However, co-immobilization of the enzyme and its co-substrate (Fc-PEG chains in this case) on viral-nanoscaffolds does induce enzymatic enhancement by promoting cooperativity between the two subunits of the homodimeric enzyme, via “synchronization” of their redox state. A decrease in substrate inhibition was also observed. This was identified as an intrinsic beneficial property of the integrated system.

Acknowldelgement

We express our gratitude to Dr. François Mavré for valuable insights and discussions regarding the kinetic behavior of PQQ-GDH.

Supplementary Material Available

Production and characterization of the Nb_{59}-GFP and GDH-Nb_{75} fusions. Assaying the degree of Fc labelling of the Fc-PEG-Nb_{59}-GFP conjugate. Adsorption isotherm of GFLV on cysteaminated gold. Cyclic voltammogram of Fc-PEG-Nb_{59}-GFP assembled on surface-adsorbed GFLV particles. Performances of some blocking agents for the nanobody-guided assembly of the enzymatic system on surface-adsorbed GFLV particles. Assaying the number of GDH-Nb_{75} per GFLV.

References

(1) Ding, S.; Cargill, A. A.; Medintz, I. L.; Claussen, J. C. Increasing the Activity of Immobilized Enzymes with Nanoparticle Conjugation. *Curr. Opin. Biotechnol.* **2015**, *34*, 242–250. https://doi.org/10.1016/j.copbio.2015.04.005.

(2) Ellis, G. A.; Díaz, S. A.; Medintz, I. L. Enhancing Enzymatic Performance with Nanoparticle Immobilization: Improved Analytical and Control Capability for Synthetic Biochemistry. *Curr. Opin. Biotechnol.* **2021**, *71*, 77–90. https://doi.org/10.1016/j.copbio.2021.06.021.

(3) Breger, J. C.; Ancona, M. G.; Walper, S. A.; Oh, E.; Susumu, K.; Stewart, M. H.; Deschamps, J. R.; Medintz, I. L. Understanding How Nanoparticle Attachment Enhances Phosphotriesterase Kinetic Efficiency. *ACS Nano* **2015**, *9*, 8491–8503. https://doi.org/10.1021/acsnano.5b03459.

(4) Brown III, C. W.; Oh, E.; Hastman, D. A.; Walper, S. A.; Susumu, K.; Stewart, M. H.; Deschamps, J. R.; Medintz, I. L. Kinetic Enhancement of the Diffusion-Limited Enzyme Beta-Galactosidase When Displayed with Quantum Dots. *RSC Adv.* **2015**, *5* (113), 93089–93094. https://doi.org/10.1039/C5RA21187E.

(5) Algar, W. R.; Malonoski, A.; Deschamps, J. R.; Blanco-Canosa, J. B.; Susumu, K.; Stewart, M. H.; Johnson, B. J.; Dawson, P. E.; Medintz, I. L. Proteolytic Activity at Quantum Dot-Conjugates: Kinetic Analysis Reveals Enhanced Enzyme Activity and Localized Interfacial "Hopping." *Nano Lett.* **2012**, *12* (7), 3793–3802. https://doi.org/10.1021/nl301727k.

(6) Wu, M.; Algar, W. R. Acceleration of Proteolytic Activity Associated with Selection of Thiol Ligand Coatings on Quantum Dots. *ACS Appl. Mater. Interfaces* **2015**, *7* (4), 2535–2545. https://doi.org/10.1021/am507466b.

(7) Vranish, J. N.; Ancona, M. G.; Walper, S. A.; Medintz, I. L. Pursuing the Promise of Enzymatic Enhancement with Nanoparticle Assemblies. *Langmuir* **2018**, *34* (9), 2901–2925. https://doi.org/10.1021/acs.langmuir.7b02588.

(8) Zhao, Z.; Fu, J.; Dhakal, S.; Johnson-Buck, A.; Liu, M.; Zhang, T.; Woodbury, N. W.; Liu, Y.; Walter, N. G.; Yan, H. Nanocaged Enzymes with Enhanced Catalytic Activity and Increased Stability against Protease Digestion. *Nat. Commun.* **2016**, *7*, 10619. https://doi.org/10.1038/ncomms10619.

(9) Johnson, B. J.; Russ Algar, W.; Malanoski, A. P.; Ancona, M. G.; Medintz, I. L. Understanding Enzymatic Acceleration at Nanoparticle Interfaces: Approaches and Challenges. *Nano Today* **2014**, No. 1, 102–131. https://doi.org/10.1016/j.nantod.2014.02.005.

(10) Claussen, J. C.; Malanoski, A.; Breger, J. C.; Oh, E.; Walper, S. A.; Susumu, K.; Goswami, R.; Deschamps, J. R.; Medintz, I. L. Probing the Enzymatic Activity of Alkaline Phosphatase within Quantum Dot Bioconjugates. *J. Phys. Chem. C* **2015**, *119*, 2208–2221. https://doi.org/10.1021/jp5110467.

(11) Rothemund, P. W. K. Folding DNA to Create Nanoscale Shapes and Patterns. *Nature* **2006**, *440* (7082), 297–302. https://doi.org/10.1038/nature04586.

(12) Wilner, O. I.; Shimron, S.; Weizmann, Y.; Wang, Z. G.; Willner, I. Self-Assembly of Enzymes on DNA Scaffolds: En Route to Biocatalytic Cascades and the Synthesis of Metallic Nanowires.

Nano Lett. **2009**, *9* (5), 2040–2043. https://doi.org/10.1021/nl900302z.

(13) Fu, J.; Liu, M.; Liu, Y.; Woodbury, N. W.; Yan, H. Interenzyme Substrate Diffusion for an Enzyme Cascade Organized on Spatially Addressable DNA Nanostructures. *J Am Chem Soc* **2012**, *134* (12), 5516–5519. https://doi.org/10.1021/ja300897h.

(14) Fu, J.; Yang, Y. R.; Johnson-Buck, A.; Liu, M.; Liu, Y.; Walter, N. G.; Woodbury, N. W.; Yan, H. Multi-Enzyme Complexes on DNA Scaffolds Capable of Substrate Channelling with an Artificial Swinging Arm. *Nat. Nanotechnol.* **2014**, *9* (7), 531–536. https://doi.org/10.1038/nnano.2014.100.

(15) Linko, V.; Eerikäinen, M.; Kostiainen, M. A. A Modular DNA Origami-Based Enzyme Cascade Nanoreactor. *Chem. Commun.* **2015**, *51* (25), 5351–5354. https://doi.org/10.1039/c4cc08472a.

(16) Ke, G.; Liu, M.; Jiang, S.; Qi, X.; Yang, Y. R.; Wootten, S.; Zhang, F.; Zhu, Z.; Liu, Y.; Yang, C. J.; Yan, H. Directional Regulation of Enzyme Pathways through the Control of Substrate Channeling on a DNA Origami Scaffold. *Angew. Chemie - Int. Ed.* **2016**, *55* (26), 7483–7486. https://doi.org/10.1002/anie.201603183.

(17) Ngo, T. A.; Nakata, E.; Saimura, M.; Morii, T. Spatially Organized Enzymes Drive Cofactor-Coupled Cascade Reactions. *J. Am. Chem. Soc.* **2016**, *138* (9), 3012–3021. https://doi.org/10.1021/jacs.5b10198.

(18) Klein, W. P.; Thomsen, R. P.; Turner, K. B.; Walper, S. A.; Vranish, J.; Kjems, J.; Ancona, M. G.; Medintz, I. L. Enhanced Catalysis from Multienzyme Cascades Assembled on a DNA Origami Triangle. *ACS Nano* **2019**, *13* (12), 13677–13689. https://doi.org/10.1021/acsnano.9b05746.

(19) Xiong, Y.; Huang, J.; Wang, S. T.; Zafar, S.; Gang, O. Local Environment Affects the Activity of Enzymes on a 3D Molecular Scaffold. *ACS Nano* **2020**, *14* (11), 14646–14654. https://doi.org/10.1021/acsnano.0c03962.

(20) Lancaster, L.; Abdallah, W.; Banta, S.; Wheeldon, I. Engineering Enzyme Microenvironments for Enhanced Biocatalysis. *Chem. Soc. Rev.* **2018**, *47* (14), 5177–5186. https://doi.org/10.1039/c8cs00085a.

(21) Abdallah, W.; Hong, X.; Banta, S.; Wheeldon, I. Microenvironmental Effects Can Masquerade as Substrate Channelling in Cascade Biocatalysis. *Curr. Opin. Biotechnol.* **2022**, *73*, 233–239. https://doi.org/10.1016/j.copbio.2021.08.014.

(22) Gao, Y.; Roberts, C. C.; Zhu, J.; Lin, J.-L.; Chang, C. A.; Wheeldon, I. Tuning Enzyme Kinetics through Designed Intermolecular Interactions Far from the Active Site. *ACS Catal.* **2015**, *5* (4), 2149–2153. https://doi.org/10.1021/acscatal.5b00130.

(23) Campbell, E.; Wheeldon, I. R.; Banta, S. Broadening the Cofactor Specificity of a Thermostable Alcohol Dehydrogenase Using Rational Protein Design Introduces Novel Kinetic Transient Behavior. *Biotechnol. Bioeng.* **2010**, *107* (5), 763–774. https://doi.org/10.1002/bit.22869.

(24) Zhang, Y.; Wang, Q.; Hess, H. Increasing Enzyme Cascade Throughput by PH-Engineering the Microenvironment of Individual Enzymes. *ACS Catal.* **2017**, *7* (3), 2047–2051. https://doi.org/10.1021/acscatal.6b03431.

(25) Azuma, Y.; Bader, D. L. V; Hilvert, D. Substrate Sorting by a Supercharged Nanoreactor. *J. Am.*

Chem. Soc. **2018**, *140* (3), 860–863. https://doi.org/10.1021/jacs.7b11210.

(26) Carette, N.; Engelkamp, H.; Akpa, E.; Pierre, S. J.; Cameron, N. R.; Christianen, P. C. M.; Maan, J. C.; Thies, J. C.; Weberskirch, R.; Rowan, A. E.; Nolte, R. J. M.; Michon, T.; Van Hest, J. C. M. A Virus-Based Biocatalyst. *Nat. Nanotechnol.* **2007**, *2*, 226–229.

(27) Cardinale, D.; Carette, N.; Michon, T. Virus Scaffolds as Enzyme Nano-Carriers. *Trends Biotechnol.* **2012**, *30*, 369-376. https://doi.org/S0167-7799(12)00050-9 [pii] 10.1016/j.tibtech.2012.04.001.

(28) Cardinale, D.; Michon, T. *Enzyme Nanocarriers*, first.; Cardinale, D., Michon, T., Eds.; Pan Stanford Publishing: Singapore, 2016.

(29) Aljabali, A. A. A.; Barclay, J. E.; Steinmetz, N. F.; Lomonossoff, G. P.; Evans, D. J. Controlled Immobilisation of Active Enzymes on the Cowpea Mosaic Virus Capsid. *Nanoscale* **2012**, *4*, 5640–5645. https://doi.org/10.1039/c2nr31485a.

(30) Minten, I. J.; Claessen, V. I.; Blank, K.; Rowan, A. E.; Nolte, R. J. M.; Cornelissen, J. J. L. M. Catalytic Capsids: The Art of Confinement. *Chem. Sci.* **2011**, *2*, 358–362. https://doi.org/10.1039/c0sc00407c.

(31) Patterson, D. P.; Schwarz, B.; Waters, R. S.; Gedeon, T.; Douglas, T. Encapsulation of an Enzyme Cascade within the Bacteriophage P22 Virus-like Particle. *ACS Chem. Biol.* **2014**, *9*, 359–365. https://doi.org/10.1021/cb4006529.

(32) Schuphan, J.; Commandeur, U. Analysis of Engineered Tobacco Mosaic Virus and Potato Virus X Nanoparticles as Carriers for Biocatalysts. *Front. Plant Sci.* **2021**, *12*, 1481. https://doi.org/10.3389/fpls.2021.710869.

(33) Rurup, W. F.; Koay, M. S. T.; Cornelissen, J. J. L. M. Viruses as Model Nanoreactors to Study Enzyme Kinetics. In *Enzyme Nanocarriers*; Cardinale, D., Michon, T., Eds.; Pan Stanford Publishing: New York, NY, 2016; pp 105–122.

(34) Patel, A. N.; Anne, A.; Chovin, A.; Demaille, C.; Grelet, E.; Michon, T.; Taofifenua, C. Scaffolding of Enzymes on Virus Nanoarrays: Effects of Confinement and Virus Organization on Biocatalysis. *Small* **2017**, *13*, 1603163. https://doi.org/10.1002/smll.201603163.

(35) Koch, C.; Wabbel, K.; Eber, F. J.; Krolla-Sidenstein, P.; Azucena, C.; Gliemann, H.; Eiben, S.; Geiger, F.; Wege, C. Modified TMV Particles as Beneficial Scaffolds to Present Sensor Enzymes. *Front. Plant Sci.* **2015**, *6*, 1137. https://doi.org/10.3389/fpls.2015.01137.

(36) Comellas-Aragonès, M.; Engelkamp, H.; Claessen, V. I.; Sommerdijk, N. A. J. M.; Rowan, A. E.; Christianen, P. C. M.; Maan, J. C.; Verduin, B. J. M.; Cornelissen, J. J. L. M.; Nolte, R. J. M. A Virus-Based Single-Enzyme Nanoreactor. *Nat. Nanotechnol.* **2007**, *2* (10), 635–639. https://doi.org/10.1038/nnano.2007.299.

(37) Pille, J.; Cardinale, D.; Carette, N.; Di Primo, C.; Besong-Ndika, J.; Walter, J.; Lecoq, H.; van Eldijk, M. B.; Smits, F. C. M.; Schoffelen, S.; van Hest, J. C. M.; Makinen, K.; Michon, T.; Mäkinen, K.; Michon, T. General Strategy for Ordered Noncovalent Protein Assembly on Well-Defined Nanoscaffolds. *Biomacromolecules* **2013**, *14*, 4351–4359. https://doi.org/10.1021/bm401291u.

(38) Patterson, D. P.; Prevelige, P. E.; Douglas, T. Nanoreactors by Programmed Enzyme Encapsulation inside the Capsid of the Bacteriophage P22. *ACS Nano* **2012**, *6* (6), 5000–5009. https://doi.org/10.1021/nn300545z.

(39) Besong-Ndika, J.; Wahlsten, M.; Cardinale, D.; Pille, J.; Walter, J.; Michon, T.; Mäkinen, K. Towards the Reconstitution of a Two-Enzyme Cascade for Resveratrol Synthesis on Potyvirus Particles. *Front. Plant Sci.* **2016**, *7*, 89. https://doi.org/10.3389/fpls.2016.00089.

(40) Cuenca, S.; Mansilla, C.; Aguado, M.; Yuste-Calvo, C.; Sánchez, F.; Sánchez-Montero, J. M.; Ponz, F. Nanonets Derived from Turnip Mosaic Virus as Scaffolds for Increased Enzymatic Activity of Immobilized Candida Antarctica Lipase B. *Front. Plant Sci.* **2016**, *7*, 464. https://doi.org/10.3389/fpls.2016.00464.

(41) Bäcker, M.; Koch, C.; Eiben, S.; Geiger, F.; Eber, F.; Gliemann, H.; Poghossian, A.; Wege, C.; Schöning, M. J.; Bäcker, M. Tobacco Mosaic Virus as Enzyme Nanocarrier for Electrochemical Biosensors. *Sensors Actuators, B Chem.* **2017**, *238*, 716–722. https://doi.org/10.1016/j.snb.2016.07.096.

(42) Milton, R. D.; Wang, T.; Knoche, K. L.; Minteer, S. D. Tailoring Biointerfaces for Electrocatalysis. *Langmuir* **2016**, *32* (10), 2291–2301. https://doi.org/10.1021/acs.langmuir.5b04742.

(43) Mazurenko, I.; Hitaishi, V. P.; Lojou, E. Recent Advances in Surface Chemistry of Electrodes to Promote Direct Enzymatic Bioelectrocatalysis. *Curr. Opin. Electrochem.* **2020**, *19*, 113–121. https://doi.org/10.1016/j.coelec.2019.11.004.

(44) De Poulpiquet, A.; Ciaccafava, A.; Lojou, E. New Trends in Enzyme Immobilization at Nanostructured Interfaces for Efficient Electrocatalysis in Biofuel Cells. *Electrochim. Acta* **2014**, *126*, 104–114. https://doi.org/10.1016/j.electacta.2013.07.133.

(45) Holzinger, M.; Le Goff, A.; Cosnier, S. Nanomaterials for Biosensing Applications: A Review. *Front. Chem.* **2014**, *2*, 63. https://doi.org/10.3389/fchem.2014.00063.

(46) Chen, H.; Simoska, O.; Lim, K.; Grattieri, M.; Yuan, M.; Dong, F.; Lee, Y. S.; Beaver, K.; Weliwatte, S.; Gaffney, E. M.; Minteer, S. D. Fundamentals, Applications, and Future Directions of Bioelectrocatalysis. *Chem. Rev.* **2020**, *120* (23), 12903–12993. https://doi.org/10.1021/acs.chemrev.0c00472.

(47) Mazurenko, I.; Monsalve, K.; Infossi, P.; Giudici-Orticoni, M. T.; Topin, F.; Mano, N.; Lojou, E. Impact of Substrate Diffusion and Enzyme Distribution in 3D-Porous Electrodes: A Combined Electrochemical and Modelling Study of a Thermostable H2/O2 Enzymatic Fuel Cell. *Energy Environ. Sci.* **2017**. https://doi.org/10.1039/c7ee01830d.

(48) Xiao, Y.; Patolsky, F.; Katz, E.; Hainfeld, J. F.; Willner, I. Plugging into Enzymes: Nanowiring of Redox Enzymes by a Gold Nanoparticle. *Science (80-.).* **2003**, *299*, 1877–1881. https://doi.org/10.1126/science.1080664.

(49) Torbensen, K.; Patel, A. N.; Anne, A.; Chovin, A.; Demaille, C.; Bataille, L.; Michon, T.; Grelet, E. Immuno-Based Molecular Scaffolding of Glucose Dehydrogenase and Ferrocene Mediator on Fd Viral Particles Yields Enhanced Bioelectrocatalysis. *ACS Catal.* **2019**, *9* (6), 5783–5796. https://doi.org/10.1021/acscatal.9b01263.

(50) Paiva, T. O.; Torbensen, K.; Patel, A. N.; Anne, A.; Chovin, A.; Demaille, C.; Bataille, L.; Michon, T. Probing the Enzymatic Activity of Individual Biocatalytic Fd-Viral Particles by Electrochemical-Atomic Force Microscopy. *ACS Catal.* **2020**, *10* (14), 7843–7856. https://doi.org/10.1021/acscatal.0c01920.

(51) Paiva, T. O.; Schneider, A.; Bataille, L.; Chovin, A.; Anne, A.; Michon, T.; Wege, C.; Demaille, C. Enzymatic Activity of Individual Bioelectrocatalytic Viral Nanoparticles: Dependence of Catalysis on the Viral Scaffold and Its Length. *Nanoscale* **2022**, *14* (3), 875–889. https://doi.org/10.1039/d1nr07445h.

(52) Revets, H.; De Baetselier, P.; Muyldermans, S. Nanobodies as Novel Agents for Cancer Therapy. *Expert Opin. Biol. Ther.* **2005**, *5* (1), 111–124. https://doi.org/10.1517/14712598.5.1.111.

(53) Wolfson, W. Ablynx Makes Nanobodies from Llama Bodies. *Chem. Biol.* **2006**, *13* (12), 1243–1244. https://doi.org/10.1016/j.chembiol.2006.12.003.

(54) Belval, L.; Hemmer, C.; Sauter, C.; Reinbold, C.; Fauny, J.-D.; Berthold, F.; Ackerer, L.; Schmitt-Keichinger, C.; Lemaire, O.; Demangeat, G.; Ritzenthaler, C. Display of Whole Proteins on Inner and Outer Surfaces of Grapevine Fanleaf Virus-like Particles. *Plant Biotechnol. J.* **2016**, *14* (12), 2288–2299. https://doi.org/10.1111/pbi.12582.

(55) Anne, A.; Moiroux, J. Quantitative Characterization of the Flexibility of Poly(Ethylene Glycol) Chains Attached to a Glassy Carbon Electrode. *Macromolecules* **1999**, *32* (18), 5829–5835. https://doi.org/10.1021/ma990560m.

(56) Anne, A.; Demaille, C.; Moiroux, J. Elastic Bounded Diffusion. Dynamics of Ferrocene-Labeled Poly(Ethylene Glycol) Chains Terminally Attached to the Outermost Monolayer of Successively Self-Assembled Monolayers of Immunoglobulins. *J. Am. Chem. Soc.* **1999**, *121*, 10379–10388. https://doi.org/10.1021/ja991780i.

(57) Hegner, M.; Wagner, P.; Semenza, G. Ultralarge Atomically Flat Template-Stripped Au Surfaces for Scanning Probe Microscopy. *Surf. Sci.* **1993**, *291* (1–2), 39–46. https://doi.org/10.1016/0039-6028(93)91474-4.

(58) Schellenberger, P.; Andret-Link, P.; Schmitt-Keichinger, C.; Bergdoll, M.; Marmonier, A.; Vigne, E.; Lemaire, O.; Fuchs, M.; Demangeat, G.; Ritzenthaler, C. A Stretch of 11 Amino Acids in the BetaB-BetaC Loop of the Coat Protein of Grapevine Fanleaf Virus Is Essential for Transmission by the Nematode Xiphinema Index. *J. Virol.* **2010**, *84* (16), 7924–7933. https://doi.org/10.1128/JVI.00757-10.

(59) Schellenberger, P.; Sauter, C.; Lorber, B.; Bron, P.; Trapani, S.; Bergdoll, M.; Marmonier, A.; Schmitt-Keichinger, C.; Lemaire, O.; Demangeat, G.; Ritzenthaler, C. Structural Insights into Viral Determinants of Nematode Mediated Grapevine Fanleaf Virus Transmission. *PLoS Pathog.* **2011**, *7* (5), e1002034. https://doi.org/10.1371/journal.ppat.1002034.

(60) Belval, L.; Marmonier, A.; Schmitt-Keichinger, C.; Gersch, S.; Andret-Link, P.; Komar, V.; Vigne, E.; Lemaire, O.; Ritzenthaler, C.; Demangeat, G. From a Movement-Deficient Grapevine Fanleaf Virus to the Identification of a New Viral Determinant of Nematode Transmission. *Viruses* **2019**, *11* (12). https://doi.org/10.3390/v11121146.

(61) Hemmer, C.; Djennane, S.; Ackerer, L.; Hleibieh, K.; Marmonier, A.; Gersch, S.; Garcia, S.; Vigne, E.; Komar, V.; Perrin, M.; Gertz, C.; Belval, L.; Berthold, F.; Monsion, B.; Schmitt-

Keichinger, C.; Lemaire, O.; Lorber, B.; Gutiérrez, C.; Muyldermans, S.; Demangeat, G.; Ritzenthaler, C. Nanobody-Mediated Resistance to Grapevine Fanleaf Virus in Plants. *Plant Biotechnol. J.* **2018**, *16* (2), 660–671. https://doi.org/10.1111/pbi.12819.

(62) Orlov, I.; Hemmer, C.; Ackerer, L.; Lorber, B.; Ghannam, A.; Poignavent, V.; Hleibieh, K.; Sauter, C.; Schmitt-Keichinger, C.; Belval, L.; Hily, J.-M.; Marmonier, A.; Komar, V.; Gersch, S.; Schellenberger, P.; Bron, P.; Vigne, E.; Muyldermans, S.; Lemaire, O.; Demangeat, G.; Ritzenthaler, C.; Klaholz, B. P. Structural Basis of Nanobody Recognition of Grapevine Fanleaf Virus and of Virus Resistance Loss. *Proc. Natl. Acad. Sci. U. S. A.* **2020**, *117* (20), 10848–10855. https://doi.org/10.1073/pnas.1913681117.

(63) Muyldermans, S. Nanobodies: Natural Single-Domain Antibodies. *Annu. Rev. Biochem.* **2013**, *82* (1), 775–797. https://doi.org/10.1146/annurev-biochem-063011-092449.

(64) Monsion, B.; Incarbone, M.; Hleibieh, K.; Poignavent, V.; Ghannam, A.; Dunoyer, P.; Daeffler, L.; Tilsner, J.; Ritzenthaler, C. Efficient Detection of Long DsRNA in Vitro and in Vivo Using the DsRNA Binding Domain from FHV B2 Protein. *Front. Plant Sci.* **2018**, *9*, 70. https://doi.org/10.3389/fpls.2018.00070.

(65) Lisdat, F. PQQ-GDH – Structure, Function and Application in Bioelectrochemistry. *Bioelectrochemistry* **2020**, *134*, 107496. https://doi.org/10.1016/j.bioelechem.2020.107496.

(66) Zhang, L.; Miranda-Castro, R.; Stines-Chaumeil, C.; Mano, N.; Xu, G.; Mavré, F.; Limoges, B. Heterogeneous Reconstitution of the PQQ-Dependent Glucose Dehydrogenase Immobilized on an Electrode: A Sensitive Strategy for PQQ Detection down to Picomolar Levels. *Anal. Chem.* **2014**, *86*, 2257–2267. https://doi.org/10.1021/ac500142e.

(67) Zevenbergen, M. A. G.; Wolfrum, B. L.; Goluch, E. D.; Singh, P. S.; Lemay, S. G. Fast Electron-Transfer Kinetics Probed in Nanofluidic Channels. *J. Am. Chem. Soc.* **2009**, *131* (32), 11471–11477. https://doi.org/10.1021/ja902331u.

(68) Bourdillon, C.; Demaille, C.; Gueris, J.; Moiroux, J.; Savéant, J.-M. A Fully Active Monolayer Enzyme Electrode Derivatized by Antigen-Antibody Attachment. *J. Am. Chem. Soc.* **1993**, *115* (i), 12264–12269. https://doi.org/10.1021/ja00079a005.

(69) Matsushita, K.; Ameyama, M. [24] d-Glucose Dehydrogenase from Pseudomonas Fluorescens, Membrane-Bound. In *Methods in Enzymology*; Academic Press, 1982; pp 149–154. https://doi.org/10.1016/S0076-6879(82)89026-5.

(70) An, R.; Moe, L. A. Regulation of Pyrroloquinoline Quinone-Dependent Glucose Dehydrogenase Activity in the Model Rhizosphere-Dwelling Bacterium Pseudomonas Putida KT2440. *Appl. Environ. Microbiol.* **2016**, *82*, 4955–4964. https://doi.org/10.1128/AEM.00813-16.

(71) Durand, F.; Limoges, B. B.; Mano, N.; Mavré, F.; Miranda-Castro, R.; Savéant, J. M.; Mavré, F.; Miranda-Castro, R.; Savéant, J.-M. Effect of Substrate Inhibition and Cooperativity on the Electrochemical Responses of Glucose Dehydrogenase. Kinetic Characterization of Wild and Mutant Types. *J. Am. Chem. Soc.* **2011**, *133* (32), 12801–12809. https://doi.org/10.1021/ja204637d.

(72) Anne, A.; Demaille, C.; Moiroux, J. Elastic Bounded Diffusion and Electron Propagation: Dynamics of the Wiring of a Self-Assembly of Immunoglobulins Bearing Terminally Attached Ferrocene Poly(Ethylene Glycol) Chains According to a Spatially Controlled Organization. *J. Am.*

Chem. Soc. **2001**, *123*, 4817–4825. https://doi.org/10.1021/ja004050f.

Graphical Table of Contents

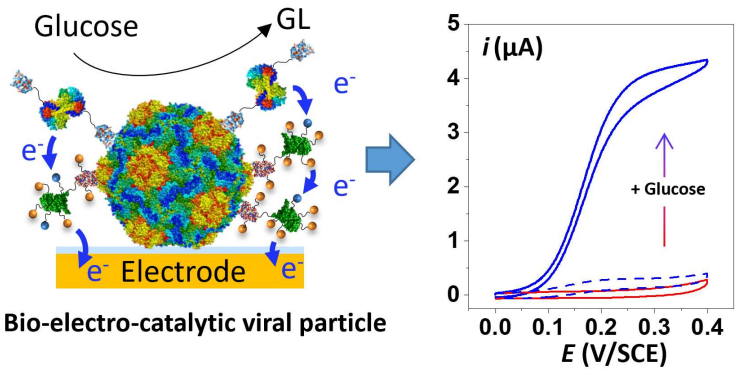

Bio-electro-catalytic viral particle